Influences of Sea Surface Temperature Gradients and Surface Roughness Changes on the Motion of Surface Oil: A Simple Idealized Study

YANGXING ZHENG

Center for Ocean–Atmospheric Prediction Studies, The Florida State University, Tallahassee, Florida

MARK A. BOURASSA AND PAUL HUGHES

Center for Ocean–Atmospheric Prediction Studies, and Department of Earth, Ocean and Atmospheric Science, The Florida State University, Tallahassee, Florida

(Manuscript received 7 August 2012, in final form 7 March 2013)

ABSTRACT

The authors' modeling shows that changes in sea surface temperature (SST) gradients and surface roughness between oil-free water and oil slicks influence the motion of the slick. Physically significant changes occur in surface wind speed, surface wind divergence, wind stress curl, and Ekman transport mostly because of SST gradients and changes in surface roughness between the water and the slick. These remarkable changes might affect the speed and direction of surface oil. For example, the strongest surface wind divergence (convergence) occurring in the transition zones owing to the presence of an oil slick will induce an atmospheric secondary circulation over the oil region, which in turn might affect the surface oil movement. SST-related changes to wind stress curl and Ekman transport in the transition zones appear to increase approximately linearly with the magnitude of SST gradients. Both surface roughness difference and SST gradients give rise to a net convergence of Ekman transport for oil cover. The SST gradient could play a more important role than surface roughness in changes of Ekman transport when SST gradients are large enough (e.g., several degrees per 10 km). The resulting changes in Ekman transport also induce the changes of surface oil movement. Sensitivity experiments show that appropriate selections of modeled parameters and geostrophic winds do not change the conclusions. The results from this idealized study indicate that the feedbacks from the surface oil presence to the oil motion itself are not trivial and should be further investigated for consideration in future oil-tracking modeling systems.

1. Introduction

On 20 April 2010, the Deepwater Horizon oil platform in the Gulf of Mexico suffered a catastrophic explosion that caused 11 deaths (Welch and Joyner 2010). This explosion created a leak in the Macondo oil well located approximately 1500 m below the sea surface, and the resulting oil spill presented an unprecedented threat to Gulf of Mexico marine resources (Robertson and Krauss 2010). Tracking the oil spill both at the surface and at depth was necessary for planning mitigation efforts and for helping coastal regions to prepare for oil beaching. Trajectory forecasts using numerical models is one method of tracking the spill. Many numerical ocean circulation models from different institutions were used for trajectory forecasting [e.g., the West Florida Shelf model (Barth et al. 2008), the Global Hybrid Coordinate Ocean Model (Global HYCOM; Chassignet et al. 2007), the Gulf of Mexico HYCOM (http://www.hycom.org), the South Atlantic Bight–Gulf of Mexico Model (SABGOM; Hyun and He 2010), the Real-Time Ocean Forecast System for the North Atlantic Ocean (RTOFS; Mehra and Rivin 2010), and the Intra-Americas Sea Nowcast/Forecast System (IASNFS; Ko et al. 2008)]. These models have been improved for tracking oil by taking advantage of the development of modern numerical models. However, their limitations were also obvious (Liu et al. 2011). For example, none of these models incorporated Stokes drift (Stokes 1880), which is a transport due to the motion of waves. Stokes drift might play an important role in the motion of an oil

Corresponding author address: Yangxing Zheng, Center for Ocean–Atmosphere Prediction Studies, The Florida State University, 2035 E. Paul Dirac Dr., Johnson Building, Tallahassee, FL 32310. E-mail: yzheng@fsu.edu

DOI: 10.1175/JAMC-D-12-0211.1

slick, particularly in the nearshore region (Hénaff et al. 2012). These forecasting models also did not consider biological consumption of oil or the physical–chemical weathering processes (Liu et al. 2011).

In this paper, surface forcing due to two small-scale processes is examined through a highly idealized simulation. One change in surface forcing occurs because of SST gradients, and the other is related to changes in surface roughness. Global and regional numerical weather prediction (NWP) models were found to underestimate the significant influence of SST on near-surface winds in regions of strong SST gradients, which is evident in Quick Scatterometer (QuikSCAT) wind fields on spatial scales shorter than 1000 km (Chelton et al. 2001, 2004, 2007; O'Neill et al. 2003, 2005; Xie 2004; Chelton 2005; Chelton and Wentz 2005; Maloney and Chelton 2006; Song et al. 2009). These studies indicated the important influences of strong SST fronts on the near-surface winds on small spatial scales. SST gradients can be strong in the transition zones between oil-free water and surface oil because oil absorbs more solar radiation because of the different thermal properties between oil and seawater. A thick oil slick was observed to exhibit an infrared signature up to several degrees Celsius warmer than the surrounding water during the Deepwater Horizon oil spill event (Svejkovsky et al. 2012). Second, physical processes affecting oil motion owing to the surface roughness discrepancy between water and oil are not fully considered in the forecast models. The sharp SST gradient and changes in surface roughness owing to the presence of an oil slick may cause additional or increased ocean–atmosphere boundary processes that can influence the motion of the oil slick itself (e.g., through the variation of Ekman transport). Numerical models for tracking oil do not consider these effects of oil on air–sea boundary processes, which ultimately affect the oil motion. This study will provide a basic understanding of how strong SST gradient and roughness changes between surface oil and surface water affect the motion of surface oil, and thus will improve oil trajectory forecasts in future modeling.

2. Model and methodology

a. UWPBL model

This study uses the University of Washington planetary boundary layer (UWPBL) model, version 4.0 (Patoux and Brown 2002; Patoux et al. 2003), to examine how temperature gradient and roughness changes between oil and surface water influence the motion of surface oil. The wind profile in the boundary layer is resolved by patching a modified Ekman spiral (Ekman-layer theory) to a logarithmic profile (surface-layer theory). The matching conditions at the patch height between the Ekman layer and the surface layer yield simple similarity relations between the surface stress and the geostrophic flow. Stratification, baroclinicity, and secondary flows can be taken into account. The so-called direct model is implemented in the experiments. If the geostrophic winds and the necessary input variables on the surface (e.g., SST, air surface temperature, humidity) are given, the direct model solves for the surface wind profile and PBL characteristics. The schematic structure of the UWPBL model for this study is shown in Fig. 1.

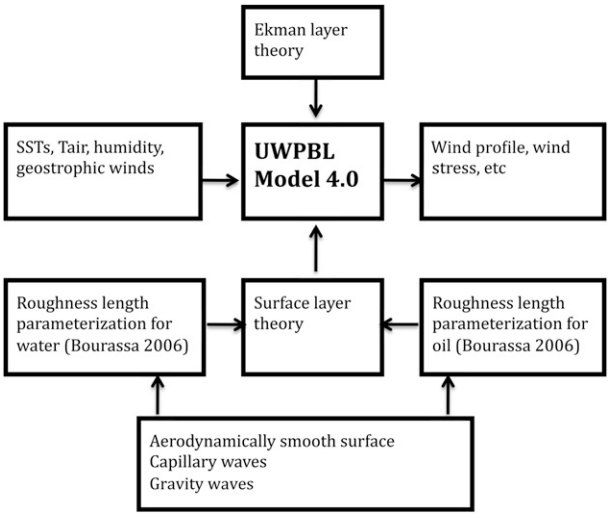

FIG. 1. Schematic structure of UWPBL model in this study.

For this study, new momentum roughness length parameterizations are embedded in the model to solve the surface water roughness and the surface oil roughness. The roughness length parameterizations for water and oil used in this model are different. For surface water roughness, the parameterization was first used in a study by Bourassa (2006), which is a modification of the Bourassa–Vincent–Wood flux model (Bourassa et al. 1999). For surface oil roughness, the roughness length in this parameterization is modified to take oil features into account. In this study, two major oil features that are different from seawater are considered: different surface roughness and the thermal properties distinguishable between oil and seawater. The model considers contributions to surface roughness from three types of surface features that include an aerodynamically smooth surface (Nikuradse 1933; Kondo 1975), capillary waves (Bourassa et al. 1999), and gravity waves (Smith et al. 1992). The roughness length parameterization equation for water/oil is

$$z_{0_i} = \beta_s \frac{0.11\nu}{|u_{*i}|} + \varepsilon \left[\left(\beta_c \frac{b\sigma}{\rho_w |\mathbf{u}_*||\mathbf{u}_* \cdot \mathbf{e}_i|} \right)^2 + \left(\beta_g \frac{a|\mathbf{u}_*||\mathbf{u}_* \cdot \mathbf{e}_i|}{g} \right)^2 \right]^{0.5},$$

where the β_s, β_c, and β_g terms are weights for the roughness length associated with an aerodynamically smooth surface, capillary waves, and gravity waves, respectively; ν is the molecular viscosity of air; and ε represents the oil damping effects on capillary waves and short gravity waves and here is set to 0.25 when oil is present for most cases. We have conducted sensitivity experiments regarding the choice of ε, for which the results are discussed in section 3f. We set ε to 1 for water; $b = 0.019$ is a dimensionless constant that is determined from laboratory observations (Bourassa et al. 1999); $a = 0.035$ is Charnock's constant; σ is surface tension, which is determined by the SST; ρ_w is water density; and g is gravitational acceleration. The roughness length is anisotropic, with unit vectors parallel $\mathbf{e}_1$ and perpendicular $\mathbf{e}_2$ to the mean direction of wave motions. The value of β_s is determined by the relation $\beta_s = 1 - \beta_g$.

The following modifications have been made from Bourassa (2006). The value of β_c is no longer restricted to 0 (no capillary waves) and 1, which was well suited for wave tanks but not for much larger spatial scales. The new value of β_c represents an average over enough space/time for a smooth transition from an aerodynamically smooth surface to a rough surface. Similarly, $\beta_g = 0$ applies only to wind waves.

For surface water, $\beta_c = 0$ and $\beta_g = 0$ for $U_{\text{eff}} < U_{\text{lim}}$; otherwise,

$$\beta_c = \tanh[0.4(U_{\text{eff}} - U_{\text{lim}})^3] \quad \text{and}$$

$$\beta_g = \tanh[0.2(U_{\text{eff}} - U_{\text{lim}})^3].$$

For surface oil, $\beta_c = 0$ and $\beta_g = 0$ for $U_{\text{eff}} < U_{\text{lim}}$; otherwise,

$$\beta_c = \tanh[0.4(U_{\text{eff}} - U_{\text{lim}})^3] \quad \text{and}$$

$$\beta_g = \tanh[0.3(U_{\text{eff}} - U_{\text{lim}})^3],$$

where $U_{\text{eff}} = u_*[\ln(z/z_0 + 1) + \varphi(z, z_0, L)]/K_v$, $\varphi(z, z_0, L)$ is a stability term, and K_v and L are von Kármán's constant and the Monin–Obukhov stability length, respectively. The term U_{lim} is a critical value that surface wind speed must reach to generate capillary waves and gravity waves on the seawater/oil surface; U_{lim} affects surface roughness through the weights for roughness length associated with capillary waves and gravity waves.

For water, $U_{\text{lim}} = 1.0\,\text{m s}^{-1}$, and for the Deepwater Horizon oil-covered region, $U_{\text{lim}} = 7.0\,\text{m s}^{-1}$. This value of U_{lim} for oil was crudely chosen based on scatterometer observations of the surface roughness of the Deepwater Horizon spill. The value of U_{lim} is not general and will vary greatly depending on the oil conditions. Further work could be done to better estimate the values of U_{lim} and ε; however, that is beyond the scope of this study. Here our goal is to show that these considerations are worthy of further analysis for at least the application of modeling oil spill trajectories.

b. Experiment design

The model domain is 27°–30°N, 90°–87°W in the Gulf of Mexico, with an idealized square-shaped oil slick located in the center of the domain (28°–29°N, 89°–88°W), roughly representing the extent of the Deepwater Horizon oil spill. The horizontal resolution is 0.04° longitude × 0.04° latitude in both water and oil. SSTs in the square-shaped oil slick are treated as spatially uniform and higher than the temperatures of the surrounding water, which are also spatially uniform. Therefore, the SST gradient is present only in the boundary between oil and water. SST gradient values at this boundary are set from zero through $0.04°\text{C}\ (0.04°)^{-1}$ at the interval of $0.001°\text{C}\ (0.04°)^{-1}$ for the experiments described in sections 3a–d. The maximum magnitude of SST gradient of $0.04°\text{C}\ (0.04°)^{-1}$ in this region is about $1°\text{C}\ (100\,\text{km})^{-1}$ for this idealized study, which is a reasonable value for strong SST gradients in open-ocean observations (O'Neill et al. 2010), though this number is much weaker than $1°–5°\text{C}\ (10\,\text{km})^{-1}$ during the Deepwater Horizon (MC-252) spill particularly (Svejkovsky et al. 2012) when thick oil is present. The results of a similar experiment using this observed higher SST gradient [i.e., $1°\text{C}\ (10\,\text{km})^{-1}$] are examined in section 3e. Near-surface air temperatures at 2 m above sea surface are assumed to be a uniform 0.5°C cooler than the sea surface. O'Neill et al. (2003, 2005, 2010) showed that the impact of atmospheric stratification is usually small relative to other considerations such as horizontal temperature gradients. The assumption that the spatial structure of SST and air surface temperature is the same is reasonable because SST is generally close to air surface temperature on such a small vertical spatial scale. Therefore, these atmospheric variables in the boundary layer are also closely associated with SST structure (i.e., SST gradient). Thus, to emphasize the role of SST gradients in the surface oil motion, we use the name "SST gradient" instead of "air temperature gradient" to describe the changes in atmospheric variables such as wind stress and wind profiles in the PBL in response to temperature gradient changes. Air humidity is $20\,\text{g kg}^{-1}$ everywhere in

the model domain. At sufficiently high wind speeds (which are infrequent over the Gulf of Mexico), the surface will roughen despite the oil; thus, oil physics will affect light and moderate winds (e.g., winds at 10-m height of less than about $8\,m\,s^{-1}$) more than strong winds (D. Long 2010, personal communication). Eastward geostrophic wind at the top of the boundary layer is about $8\,m\,s^{-1}$, which is determined by an air pressure field in which air pressure difference in the neighboring grids is set to 2.845 Pa. The surface winds are much lighter than this geostrophic wind. The major parameters and variables for experiments are listed in Table 1.

On the basis of the surface roughness parameterization equation, ε has no impact for oil surface if the simulated surface wind speed U_{eff} is less than $7\,m\,s^{-1}$ because the capillary waves and short gravity waves are thoroughly suppressed. Although high wind speeds are not frequent over the Gulf of Mexico, we also perform a high wind speed case in which the epsilon has an impact on surface roughness with a variety of SST gradients. For the high wind speed case, we also conduct a series of sensitivity experiments (section 3f) with

TABLE 1. Model domain and key input variables. Here, Δx is grid distance in degrees of longitude, Δy is grid distance in degrees of latitude, U_{geo} is eastward geostrophic wind, SST is sea surface temperature, T_{air} is surface air temperature, and ΔT is temperature difference in the boundary between surface oil and surface seawater.

Model domain:	Air humidity = $20\,g\,kg^{-1}$
27°–30°N, 90°–87°W	
Oil domain:	SST = 25°C for water
28°–29°N, 89°–88°W	SST = 25°C + ΔT for oil
Resolution:	T_{air} = 24.5°C for water
$\Delta x \times \Delta y = 0.04° \times 0.04°$	T_{air} = 24.5°C + ΔT for oil
$U_{\text{geo}} = 8\,m\,s^{-1}$	ΔT = 0.001°, 0.002°, . . . , 0.04°C

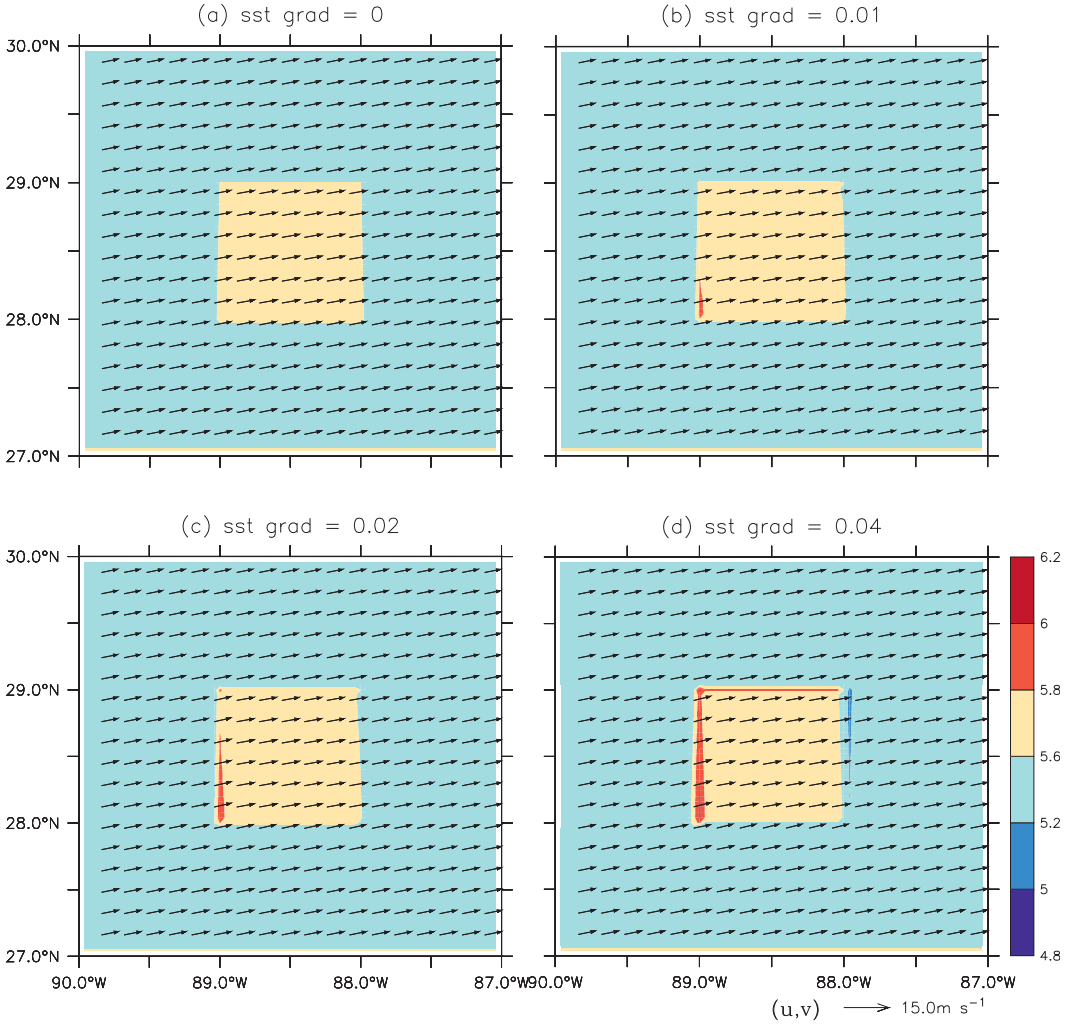

FIG. 2. Surface wind speeds (shaded contours; $m\,s^{-1}$) and surface winds (vectors; $m\,s^{-1}$) for SST gradients of (a) 0°, (b) 0.01°, (c) 0.02°, and (d) 0.04°C $(0.04)^{-1}$.

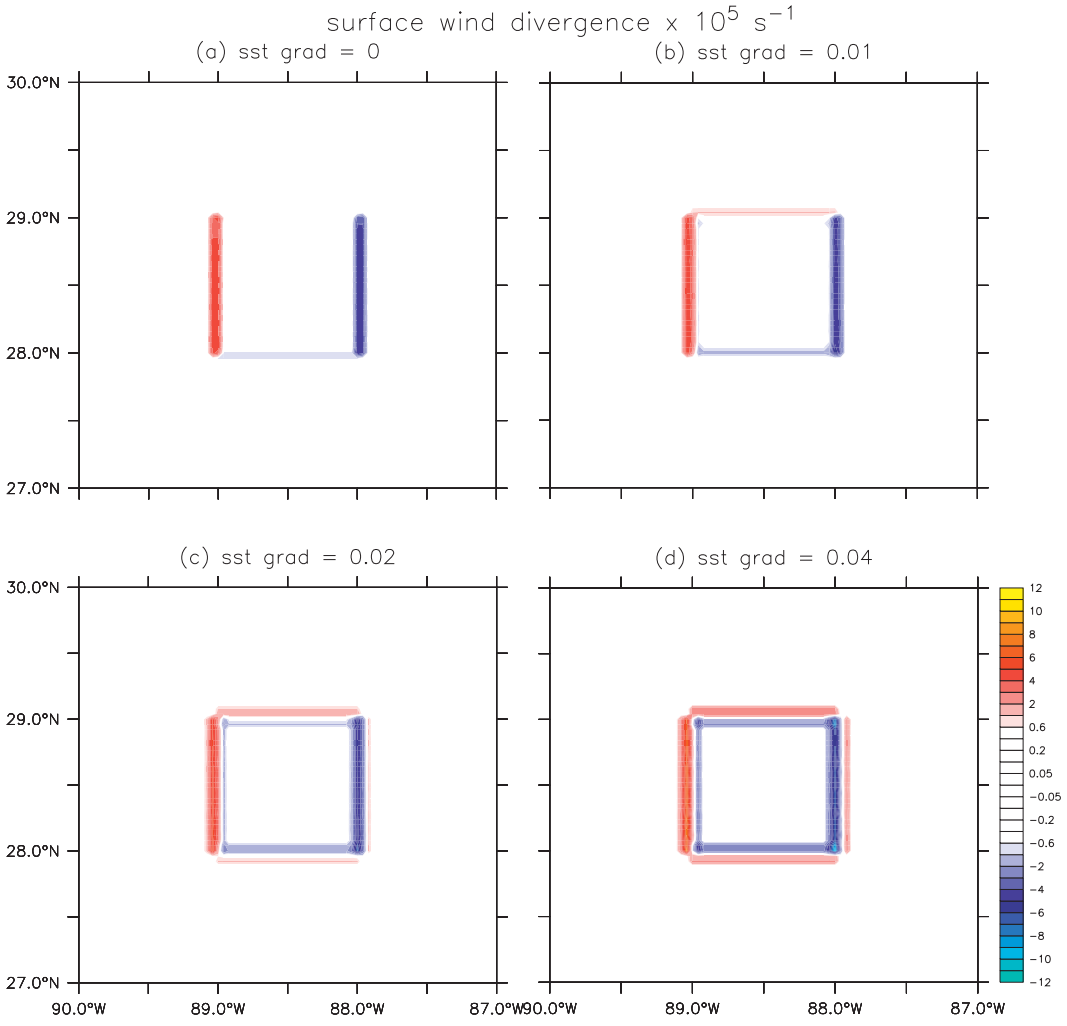

FIG. 3. Surface wind divergences (shaded contours; s^{-1}) for SST gradients of (a) 0°, (b) 0.01°, (c) 0.02°, and (d) 0.04°C $(0.04°)^{-1}$.

varying choices of ε but without the impact of an SST gradient.

3. Results

a. *Changes in surface wind speed and wind divergence*

The distributions of surface wind speed and wind vectors (Fig. 2) are shown for several SST gradients. Surface wind speeds over the water (hereinafter meaning water away from the oil boundary) and oil interior fall within 5.2–5.6 and 5.6–5.8 m s^{-1}, respectively. The difference in wind speed between water interior and oil interior is primarily caused by the different roughness for water and oil; the oil slick strongly dampens the surface water waves that dominate the roughness.

However, more attention is paid to the changes in the boundary between oil and water because the SST gradients can be significantly large in the transition zones. The surface wind speed changes sharply because of the strong SST gradient. For example, in the western boundary shown in Fig. 2d, the surface wind speed is close to 6 m s^{-1}, which is larger than wind speeds over both the water and the oil interior (as more clearly seen in Fig. 4a). The direction of surface winds is also changed in the transition zones (as more clearly seen in Fig. 8a). These changes in the transition zones are primarily caused by strong SST gradients; however, the change in surface wind speed associated with changing roughness also modifies the Coriolis force and the wind direction. The turning angle, the change in wind direction between surface winds and eastward geostrophic winds at the top of the boundary layer, is modified in the UWPBL according to Ekman spiral theory (Ekman 1905).

Surface wind divergence plays a role in the movement of surface oil by inducing an overlying atmospheric

secondary circulation in the boundary layer. The distribution of surface wind divergence in response to different SST gradients (Fig. 3) demonstrates the importance of SST gradients to the strength of surface wind divergence. The surface wind divergence is evident only in the transition zones. The magnitude of surface wind divergence is strongest where the winds blow roughly perpendicular to isotherms, as in the west and east boundaries for this idealized study. The surface wind divergence (convergence) dominates in the regions of downwind (upwind) SST gradients. These horizontal motions would induce an atmospheric secondary circulation, which in turn would affect the surface oil movement. The surface wind divergence (convergence) appears much weaker in the regions of crosswind SST gradients (i.e., southern and northern boundaries). No obvious surface wind divergence exists in the water and the oil interior because no SST gradient or roughness difference exists there, and our simple model does not explicitly simulate the atmospheric secondary circulations. Interestingly, the changes in surface roughness appear to play a more important role in surface wind speed and surface wind divergence relative to the SST gradients in our experiments when the SST gradients are smaller than 1°C $(100\,\text{km})^{-1}$ (Figs. 4a,b). In section 3e, we will investigate a case of stronger SST gradients and further discuss the relative roles of SST gradients and surface roughness changes. The strong surface wind divergence in the transition zones can be caused by changes in both the magnitude and the direction of surface winds. Note that the changes in surface wind divergence due to the latitudinal dependence of the Coriolis force are small in comparison with those induced by SST gradients and changes in surface roughness.

Changes of surface wind speed and divergence along 28.56°N are shown for different downwind SST gradients. We see the expected roughness-related increase of surface wind speed as the air moves from water to oil surface. Surface wind speed also increases in the transition zone in response to positive downwind SST gradients (Fig. 4a). The change in surface wind speed and wind direction by SST gradients is primarily from a contribution of a thermal wind correction to the classical Ekman spiral. A thermal wind correction can make a contribution to surface winds (usually represented by winds at 10 m above sea surface) depending on the angle between the geostrophic winds and the orientation of the SST gradient. Thus, wind speed will decrease if the geostrophic winds are over the negative downwind SST gradient (not shown). As seen in previous work (e.g., Chelton et al. 2004; O'Neill et al. 2010), the surface wind divergence becomes stronger as the SST gradient increases. Our results show that there exist relatively large

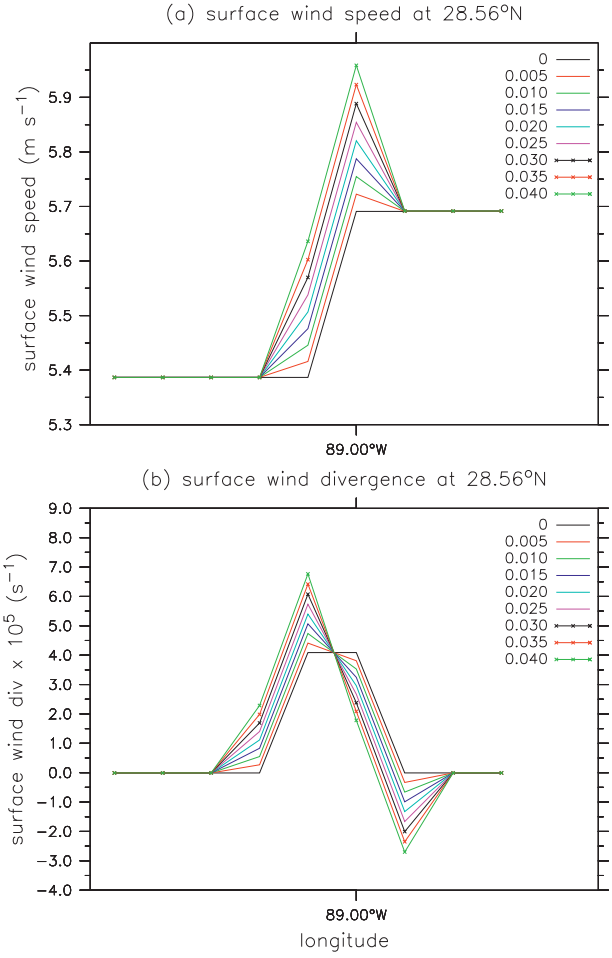

FIG. 4. (a) Surface wind speeds (m s^{-1}) and (b) surface wind divergences (s^{-1}) along 28.56°N for various SST gradients [°C (0.04°)$^{-1}$].

positive values of surface wind divergence in the transition zone owing to surface roughness changes and the existence of a strong SST gradient.

b. *Changes in wind stress curl*

The changes in magnitude and direction of wind stress modify Ekman transport and hence modify the oil motion. The pattern and magnitude of wind stress curl and wind stress vectors (Fig. 5) are shown in response to different SST gradients. The magnitude of wind stress curl is strongest in the transition zones where winds blow roughly parallel to isotherms, shown here in the southern and northern bounds. It is relatively weak in the eastern and western boundaries. Negative (positive) curl dominates in the western and northern (eastern and southern) boundaries. Our simple modeling results concerning the influence of SST fronts on near-surface winds are consistent with previous observational studies (e.g., Chelton 2005) except that we have also taken into

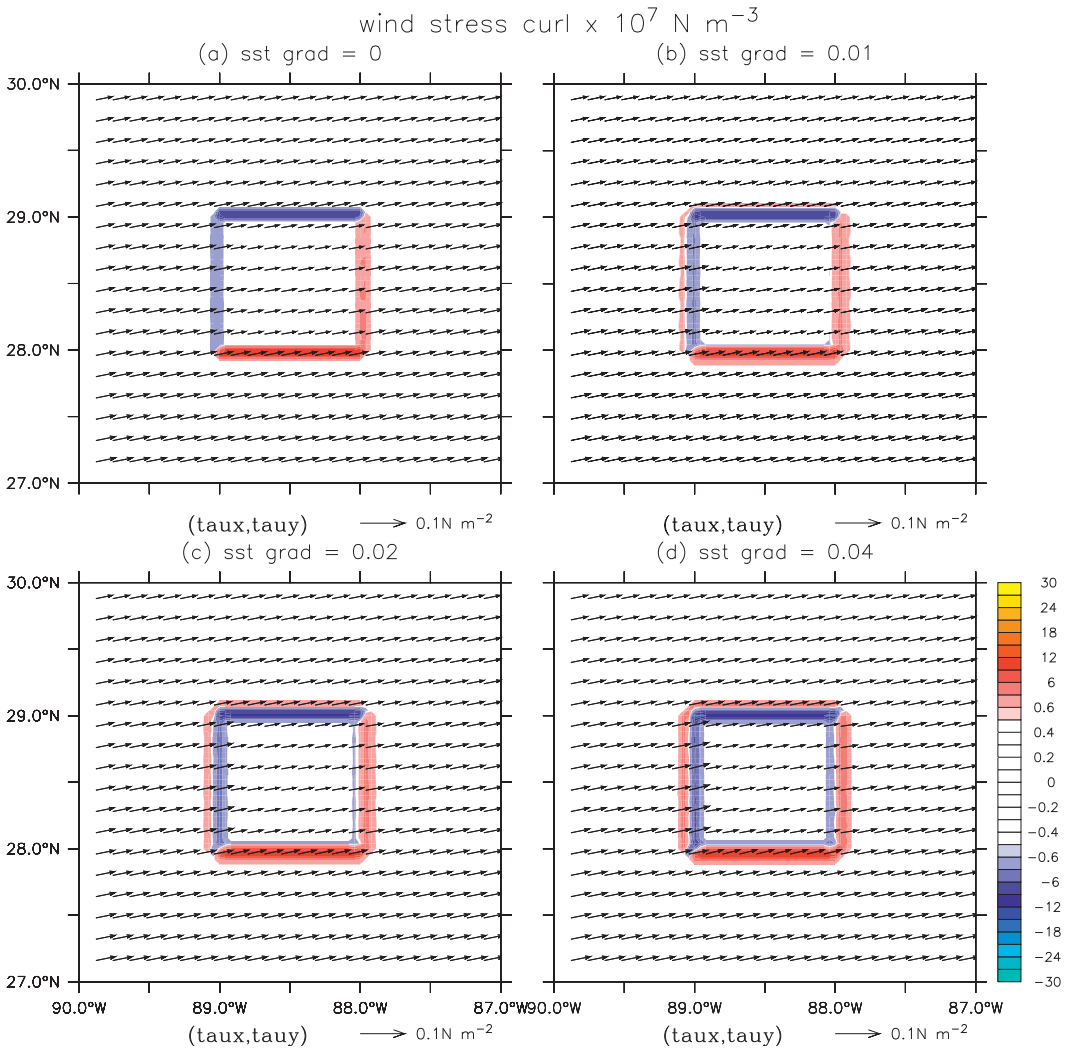

FIG. 5. Wind stress curls (shaded contours; N m^{-3}) and wind stress (vectors; N m^{-2}) for SST gradients of (a) 0°, (b) 0.01°, (c) 0.02°, and (d) 0.04°C (0.04°)$^{-1}$.

account the influence of oil's modification of surface roughness. Again the change in surface roughness also plays an essential role in the change of wind stress curl. It is expected that the wind stress curl over the water and oil interior is negligible because no SST gradient or roughness difference exists far away from the transition zones.

c. *Ekman transport of mass*

It is well known that horizontal Ekman transport of mass in the ocean Ekman layer is entirely determined by the imposed wind stress, and is defined by

$$M_x = \tau_y / f \quad \text{and} \tag{1}$$

$$M_y = -\tau_x / f, \tag{2}$$

where M_x and M_y represent the zonal and meridional mass transports (kg m^{-1} s^{-1}), τ_x and τ_y represent the zonal and meridional wind stress components, and f is the Coriolis parameter.

To understand how the SST gradients affect Ekman transport, we compute the zonal and meridional Ekman transport of mass relative to that without the influence of SST gradients (Fig. 6), so that the surplus transports are mainly caused by the strong SST gradients in the transition zones between water and slick. There is a net eastward (westward) transport in the western (eastern) transition zone and a much weaker net southward (northward) transport in the northern (southern) transition zone. Thus, there is a net convergence of transport. There are strong net meridional transports in four boundaries since change in τ_x is large in response to large idealized SST gradient changes. This convergence results in a net shrinking of the oil slick and downward movement below the surface slick. There is a cyclonic

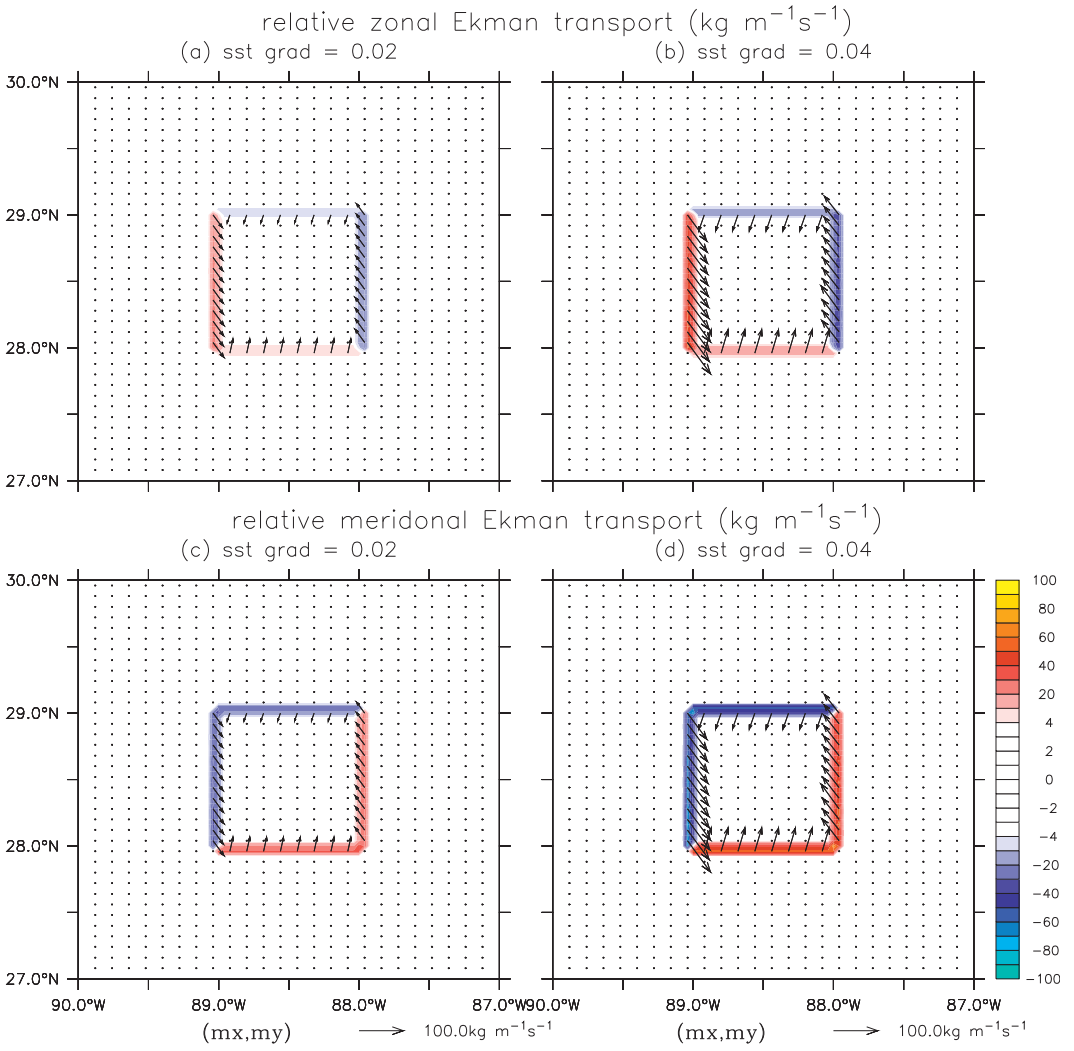

FIG. 6. Zonal Ekman transport of mass relative to zero SST gradient (shaded contours; kg m^{-1} s^{-1}) and total Ekman mass transport (vectors; kg m^{-1} s^{-1}) for SST gradients of (a) 0.02° and (b) 0.04°C (0.04°)$^{-1}$. (c),(d) As in (a),(b), but for meridional Ekman mass transport.

rotation of Ekman transport owing to the strong SST front that distorts and rotates the oil slick.

The detailed structure of zonal and meridional Ekman transport is examined as a function of downwind/crosswind SST gradient changes and surface roughness changes, particularly near the transition zones (Fig. 7). The meridional transport at 88.44°W (Fig. 7a) and zonal transport at 28.56°N (Fig. 7b) in response to five different SST gradients are examined. A sharp decrease (increase) of meridional transport occurs around 28°N (29°N) that is caused by the marked changes of roughness and strong crosswind SST gradients. Southward transport decreases from 600 to 480 kg m^{-1} s^{-1} around 28°N owing to a roughness shift from water to oil slick. There is a further decrease around 28°N from 480 to 440 kg m^{-1} s^{-1}, for example, owing to an SST gradient of 0.02°C (0.04°)$^{-1}$. The changes at 29°N can be explained in a similar way. Zonal Ekman transport in response to a downwind SST gradient and roughness change along 28.56°N behaves in a similar way except that the slope of the curve is zero because there is no change in the Coriolis parameter along the same latitude. Also the resultant zonal transport due to the downwind SST gradient is comparable to that due to the surface roughness change. Nevertheless, both roughness shift and the presence of strong SST gradients play an important role in the remarkable changes to Ekman transport in the transition zones. A more complex model is required to examine the propagation of these changes.

Changes in Ekman transport shown in Fig. 7 can be caused by the changes in both the magnitude and the direction of wind stress; thus, we compare the wind

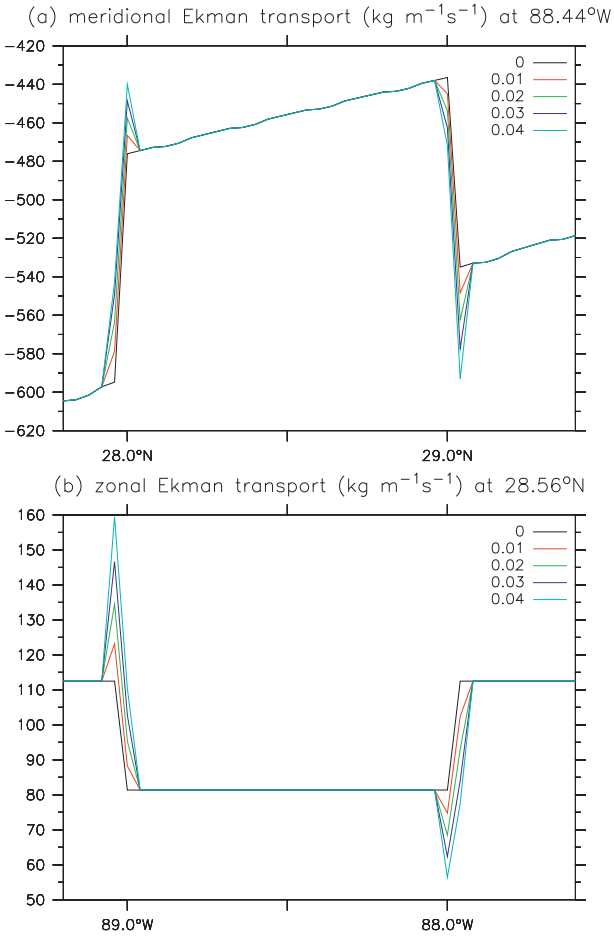

FIG. 7. (a) Meridional Ekman transport of mass along 88.44°W (kg m^{-1} s^{-1}) for five cases with various SST gradients [°C (0.04°)$^{-1}$]. Negative values represent southward transport. (b) Zonal Ekman mass transport along 28.56°N for five cases with various SST gradients [°C (0.04°)$^{-1}$].

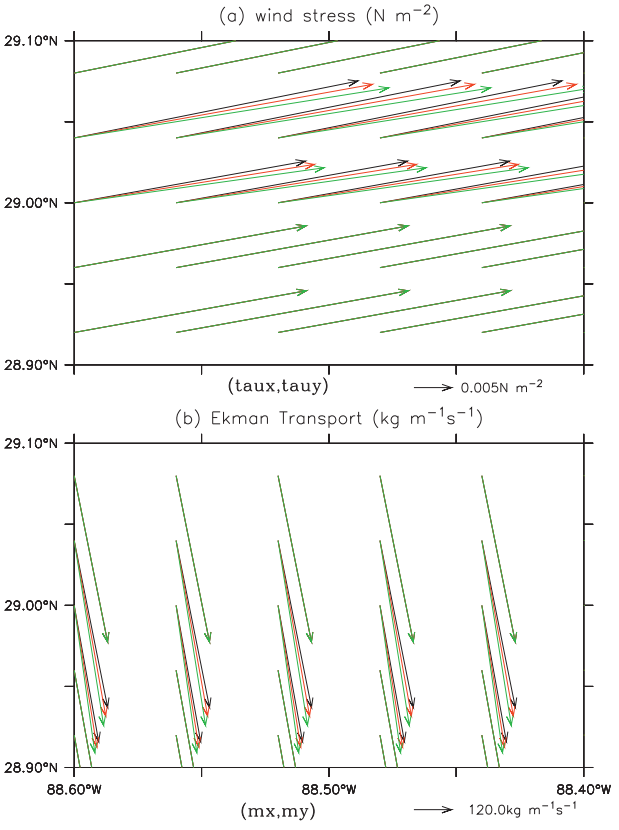

FIG. 8. (a) Wind stress vector (N m^{-2}) and (b) Ekman mass transport (kg m^{-1} s^{-1}) for three cases with various SST gradients. Black, red, and green represent SST gradients equal to 0°, 0.02°, and 0.04°C (0.04°)$^{-1}$, respectively. Note that in the regions away from the boundary, black and red are completely overlapped by green, indicating identical values in these regions.

stress vectors and Ekman transport vectors near 29°N for three SST gradients [e.g., 0°, 0.02°, and 0.04°C (0.04°)$^{-1}$] (Fig. 8). It is clear that wind stress rotates clockwise and strengthens in response to increasing SST gradients in the transition zones. Accordingly, the Ekman transport rotates clockwise and strengthens in response to increasing SST gradients in the transition zones. Therefore, changes in both magnitude and direction of wind stress from the strength of strong SST fronts and sharp roughness shift may contribute to the speed and direction of surface oil movement by Ekman transport.

d. Ekman transport and wind stress curl dependence on SST gradients

Since surface oil movement is closely linked to Ekman transport (Fig. 6) and wind stress curl, it is necessary to assess the relationship among Ekman transport, wind stress curl, and SST gradients to understand how different SST gradients affect the surface oil motion. For this purpose, we show in Fig. 9 how Ekman transports respond to different SST gradients in four boundaries of the oil slick. Since there are tiny latitudinal (longitudinal) variations of peak Ekman transport of mass in the western and eastern (northern and southern) boundaries, a location near the middle portion of each boundary is arbitrarily chosen. Figures 9a and 9b capture the relation between zonal Ekman mass transport and SST gradient at a location in the western (eastern) boundaries. Only the differences between the actual Ekman transport for nonzero SST gradients and the actual Ekman transport for zero SST gradients are shown so that the contribution from surface roughness change is excluded, given that changes in SST gradients are separable from changes in surface roughness in physics. It is evident that Ekman transport from water to oil slick is enhanced in response to an SST gradient increase in

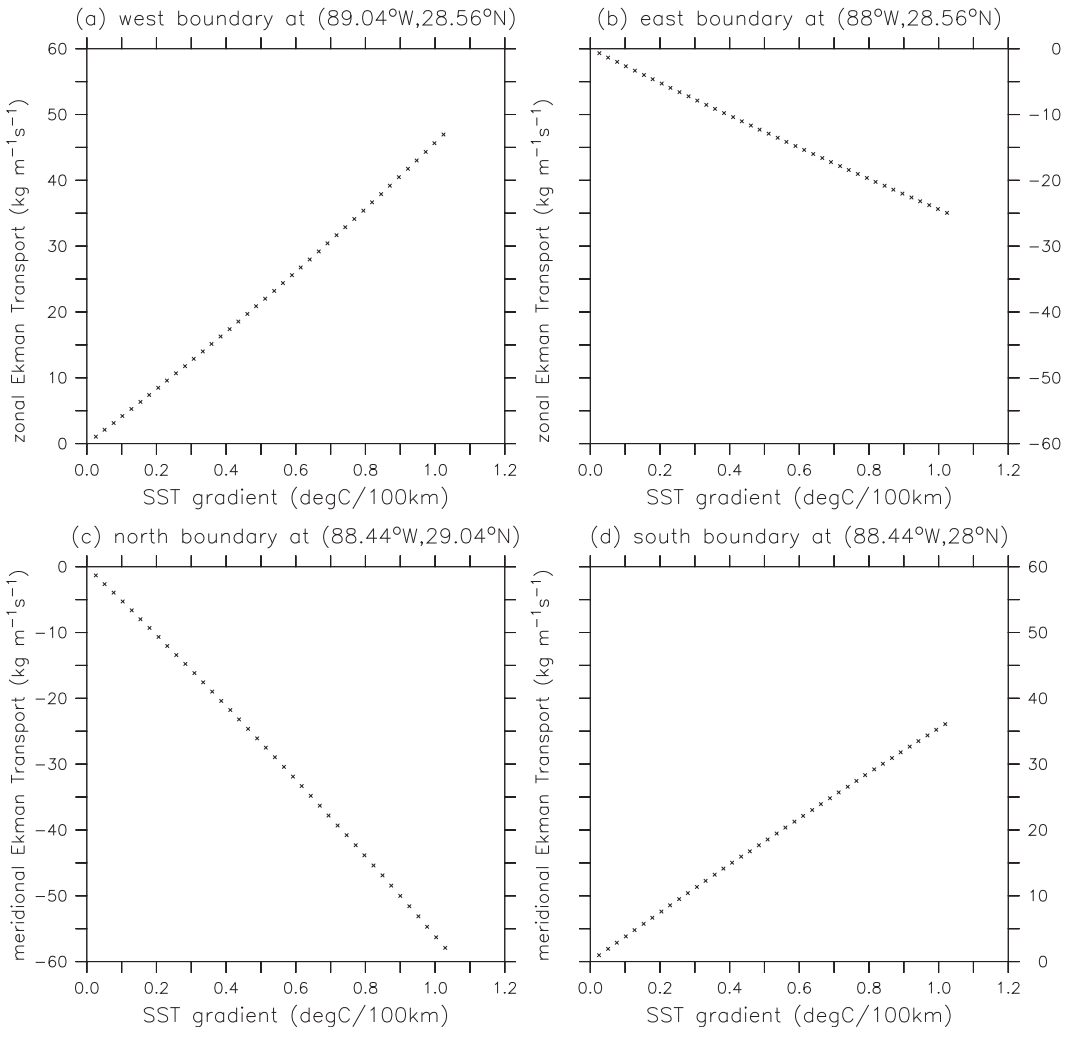

FIG. 9. Zonal Ekman transport of mass ($\mathrm{kg\,m^{-1}\,s^{-1}}$) relative to zero SST gradient for various SST gradients [°C $(100\,\mathrm{km})^{-1}$] in (a) western boundary at (28.56°N, 89.04°W), (b) eastern boundary at (28.56°N, 88°W), and meridional Ekman mass transport ($\mathrm{kg\,m^{-1}\,s^{-1}}$) relative to zero SST gradient for various SST gradients [°C $(100\,\mathrm{km})^{-1}$] in (c) northern boundary (29.04°N, 88.44°W), and (d) southern boundary at (28°N, 88.44°W). Positive (negative) values in (a) and (b) represent strengthened (weakened) eastward Ekman transport. Negative (positive) values in (c) and (d) represent strengthened (weakened) southward Ekman transport.

the transition zone between water and oil. This approximately linear relationship implies that a stronger SST frontal zone can produce a greater Ekman transport from water to oil. The modeled zonal Ekman transport from oil to water in the eastern boundary is weakened in response to an SST gradient increase, also with an approximate linear relationship. Similarly, there is a stronger southward Ekman transport in the northern boundary and a weaker southward Ekman transport in the southern boundary in response to an SST gradient increase with an approximate linear relationship (Figs. 9c,d). Both zonal and meridional transports in each boundary result in a stronger net convergence of Ekman transport in the oil region when the SST gradients in the transition zone are greater. In addition, the atmospheric secondary circulation induced by surface wind divergence (convergence) in the oil–water boundary would also modify the transport.

As it was seen in Fig. 5 that wind stress curl depends on SST gradients, the above relationship between Ekman transport and SST gradient is closely tied to the dependence of wind stress curl on SST gradient (Fig. 10). Since negative (positive) wind stress curl dominates in the western and northern (eastern and southern) boundaries (Fig. 5), both negative (positive) slopes in the western and northern (eastern and southern) boundaries imply a linear increase of the wind stress curl in magnitude to an SST gradient increase. This result is consistent with the

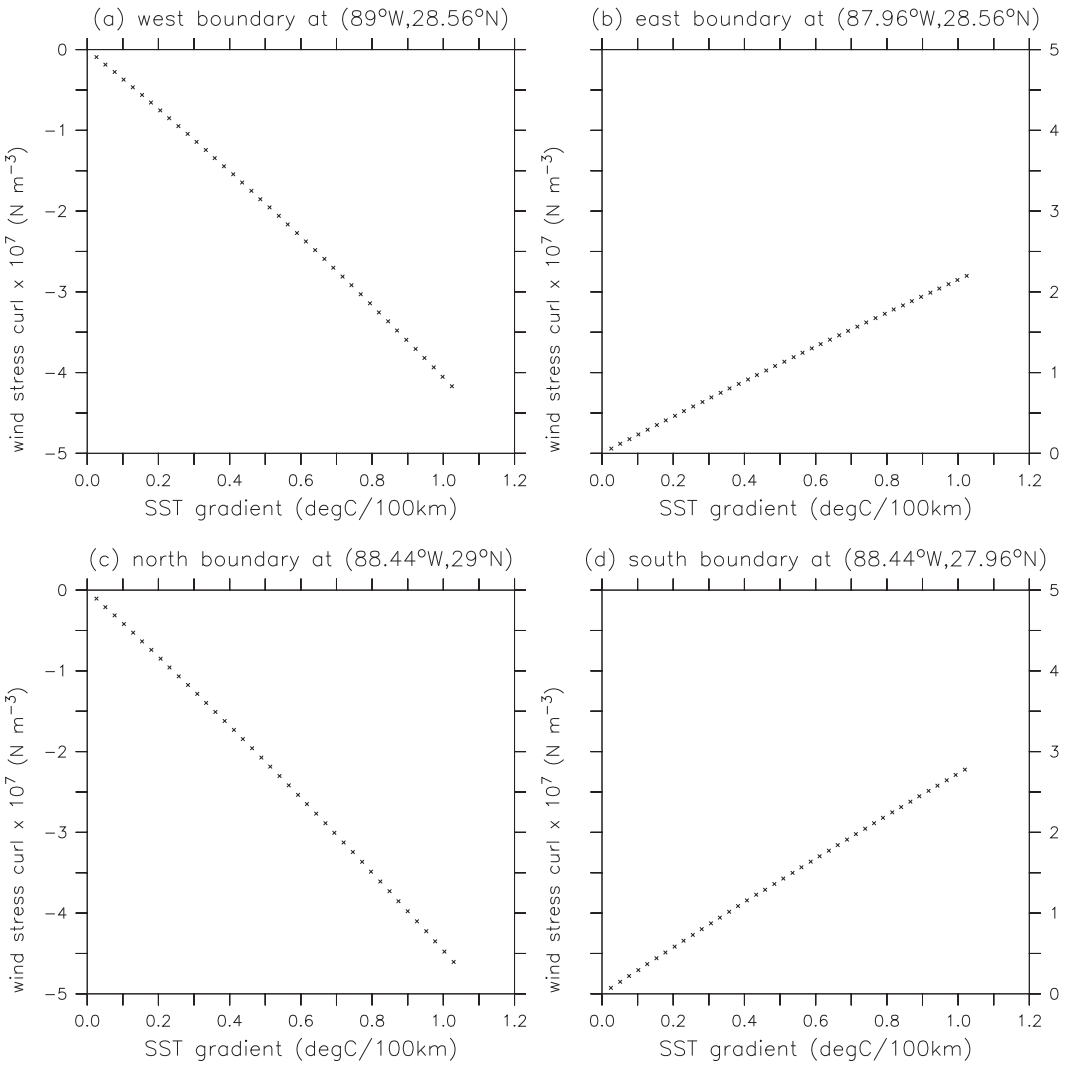

FIG. 10. Curl of wind stress ($N\,m^{-3}$) relative to zero SST gradient for various SST gradients [°C $(100\,km)^{-1}$] in (a) western boundary at (28.56°N, 89°W), (b) eastern boundary at (28.56°N, 87.96°W), (c) northern boundary at (29°N, 88.44°W), and (d) southern boundary at (27.96°N, 88.44°W). Both a negative slope in (a) and (c) and a positive slope in (b) and (d) represent a strengthened magnitude of wind stress curl in a linear response to an SST gradient increase.

result of a previous observational study without oil (Chelton et al. 2004). Thus, strong SST gradients can significantly influence surface oil motion through producing changes in wind stress curl and Ekman transport.

e. *Relative role of SST gradient and surface roughness change*

The previous results (sections 3a–d) are obtained from the model with SST gradients within 1°C $(100\,km)^{-1}$. A recent observational study (Svejkovsky et al. 2012) indicated SST gradients of 1°–5°C $(10\,km)^{-1}$ between water and oil in some cases during the Deepwater Horizon spill. These SST gradients are not uncommon in coastal regions (e.g., Walker et al. 2005) or regions associated with the Gulf Stream in the Atlantic Ocean, the Loop Current in the Gulf of Mexico, and the Kuroshio Extension in the Pacific Ocean, especially in cooler seasons (e.g., Warner et al. 1990). To identify the relative role of SST gradients and surface roughness in surface winds and oceanic Ekman transport, we perform an experiment in which the same winds, water temperature, and humidity are applied with a more realistic SST gradient of 0.4°C $(0.04°)^{-1}$ [i.e., about 1°C $(10\,km)^{-1}$] in the boundary between the oil and the water surface. The results show that along 28.16°N, an SST gradient of 1°C $(10\,km)^{-1}$ produces a more pronounced change in surface wind speed, surface wind divergence, and zonal oceanic Ekman transport than do surface roughness change and an SST

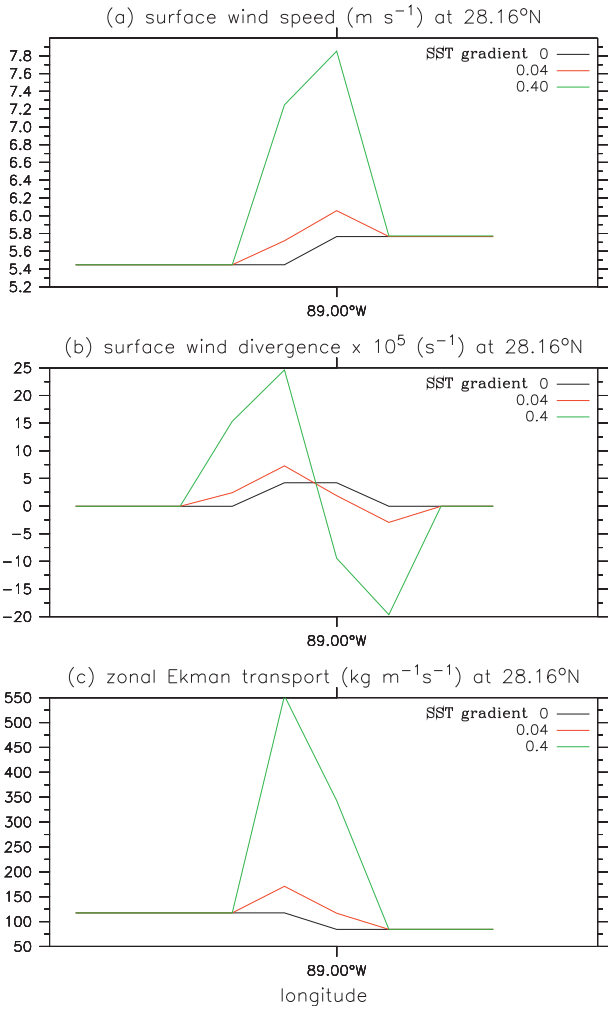

FIG. 11. (a) Surface wind speeds (m s^{-1}), (b) surface wind divergences (s^{-1}), and (c) zonal Ekman transport along 28.16°N for an extreme SST gradient of 0.4°C (0.04°) [~1°C (10 km)$^{-1}$, similar to SST gradients observed during the Deepwater Horizon (MC-252) spill] in comparison with a relatively small SST gradient and no SST gradient.

gradient of 1°C (100 km)$^{-1}$ in the transition zone (Fig. 11). Thus, extremely large SST gradients have a greater impact than surface roughness changes on surface winds and oceanic Ekman transport, and hence, on the oil's movement. Therefore, conclusions about the relative role of SST gradient and surface roughness changes in the oil's motion could be dependent on the magnitude of SST gradient and the amount of surface motion damped by the oil.

f. Analysis of sensitivity experiments forced by a high wind

Our results (sections 3a–e) are obtained from the model that is forced by a low geostrophic wind (8 m s^{-1}), which produces a low surface wind speed (less than 7 m s^{-1}) that occurs frequently in the Gulf of Mexico. In this section, results from a series of experiments for high wind speed are discussed. The same model inputs including SST gradients within 1°C (100 km)$^{-1}$, except for a higher uniform eastward geostrophic wind (12 m s^{-1}), are used in the UWPBL model. This geostrophic wind is expected to produce a surface wind speed larger than 7 m s^{-1}. On the basis of the surface roughness parameterization method used for this study, the results should be dependent on the parameter of ε. We first test how the surface processes respond to varying SST gradients for this high-wind case given the same ε as used in previous sections. Furthermore, we conduct a series of experiments to examine how the surface processes are sensitive to the choice of ε in the surface roughness parameterization.

Similar results regarding spatial pattern in surface winds and wind speed, wind stress, and Ekman transport are reproduced (not shown). Here the relative roles of surface roughness and SST gradients in surface wind speed (thus wind stress and oceanic Ekman transport) are demonstrated (Fig. 12). Figure 12a indicates that surface wind speeds at 28.56°N, 89°W become stronger as the downwind SST gradients increase. The magnitude of surface wind speed reaches 8.7 m s^{-1} when the SST gradient is equal to 0.04°C (0.04°)$^{-1}$ [i.e., about 1°C (100 km)$^{-1}$, a large value]. However, a maximum wind speed change caused by the SST gradients is only 0.3 m s^{-1}. This number is smaller than the wind speed change of 0.8 m s^{-1} that is produced by the change of surface roughness from water to oil. How surface wind speeds respond to the magnitude of ε alone is also investigated (Fig. 12b). It is evident that the magnitude of surface wind speed is not greatly affected by the choice of ε since a maximum wind speed change related to the selection of ε is only 0.23 m s^{-1}. Thus, the ε-related wind speed change is much smaller than the surface wind speed change of 0.7 m s^{-1} caused by the surface roughness shift. This indicates that the roughness-induced surface wind speed is not greatly dependent on the selection of ε. Therefore, our major conclusions expressed in previous subsections (sections 3a–d) are not subject to the selection of ε and the choice of 0.25 for ε in the model is appropriate. Another interesting result is that the SST gradient-related surface wind speed is approximately linear with the magnitude of the downwind SST gradient (Fig. 12c) and the ε-related surface wind speed is not linear with the magnitude of ε (Fig. 12d).

4. Summary

This study uses the UWPBL model to examine how changes in SST gradient and surface roughness influence the motion of an oil slick. We examine changes to surface

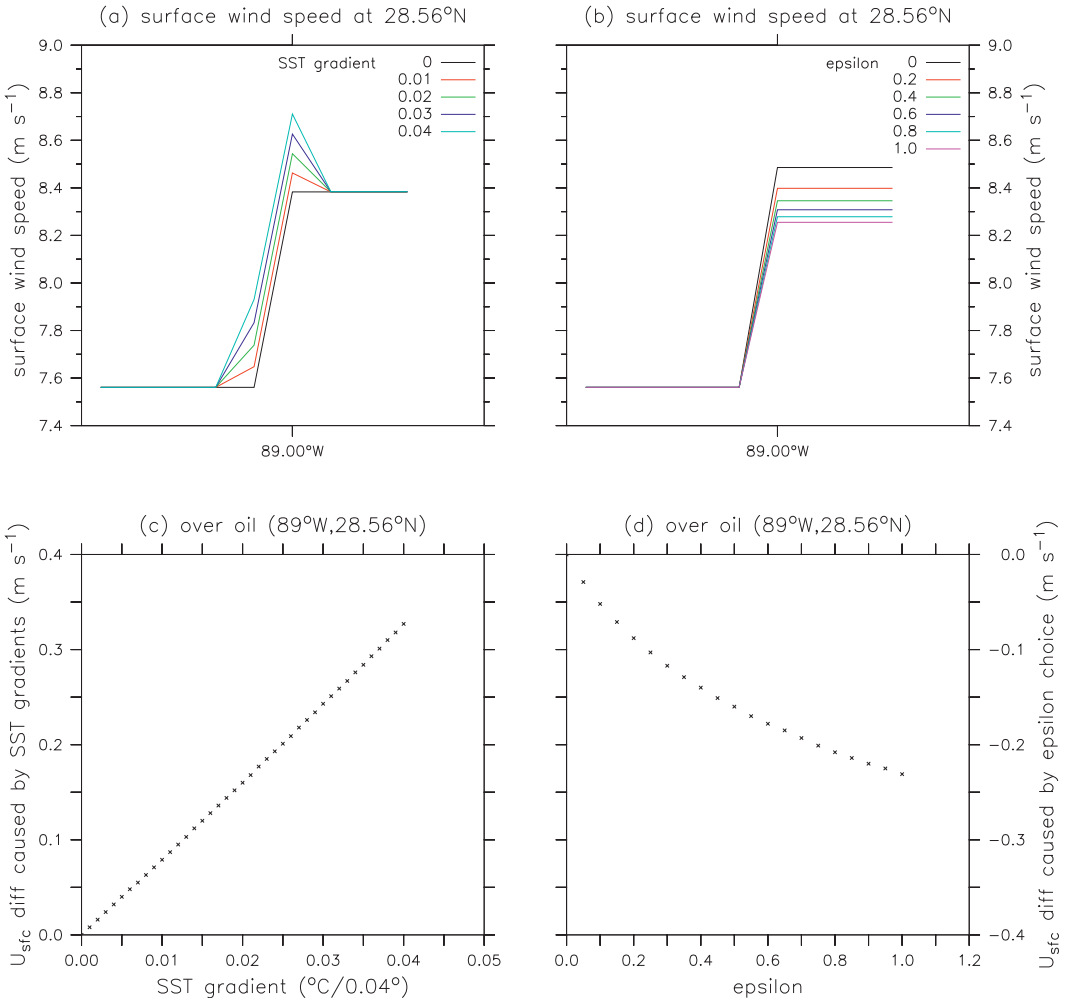

FIG. 12. (a) Surface wind speeds ($m\,s^{-1}$) around 28.56°N, 89°W for various SST gradients [°C $(0.04°)^{-1}$] given that ε is set to 0.25, (b) surface wind speeds ($m\,s^{-1}$) around 28.56°N, 89°W for various ε given that SST gradient is set to zero, (c) surface wind speeds ($m\,s^{-1}$) at 28.56°N, 89°W relative to zero SST gradient for various SST gradients, and (d) surface wind speeds at 28.56°N, 89°W relative to that when $\varepsilon = 0$ for different magnitudes of ε. The experiments are forced by eastward geostrophic winds of $12\,m\,s^{-1}$.

wind speed and divergence, wind stress curl, and Ekman transport in the transition zones between water and oil because these factors may affect the surface oil movement. Changes in surface wind speed and in wind stress over the water and oil interior are expected because of the surface roughness difference between the two media. Model results suggest that nontrivial surface transport due to the influence of strong SST gradients and changes in surface roughness could be important to the motion of the oil slick itself. The overlying atmospheric secondary circulation induced by surface wind divergence, and oceanic secondary circulation related to Ekman transport induced by a change in wind stress curl, exist because of the oil slick. Both the direction and speed of surface oil movement are closely associated with the strength of the SST gradient between surface water and surface oil. SST-related changes to wind stress curl and Ekman transport in the transition zones appear to increase approximately linearly to the magnitude of SST gradients. A faster Ekman transport across western and northern boundaries and a slower Ekman transport across southern and eastern boundaries driven by uniform eastward winds and strong SST gradients produce a net convergence in the surface oil area, which can cause contraction of the surface oil. The surface roughness change appears to play a more important role than SST gradients in changes of oceanic Ekman transport in the crosswind SST gradient region when the SST gradients are smaller than 1°C $(100\,km)^{-1}$. However, SST gradients could play a more important role than surface

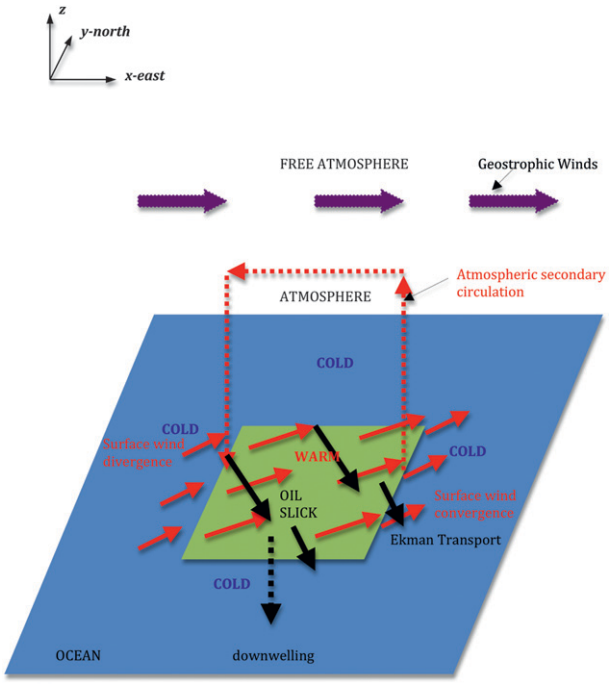

FIG. 13. 3D schematic diagram depicting the induced atmospheric secondary circulation and downwelling of oil under the influence of SST gradient in the boundary between an oil slick (green shading) and water (blue shading). Oil slick temperature is spatially homogeneous and higher than the water temperature, which is also spatially homogeneous. Near-surface air temperature is 0.5°C lower than SST in the water and the oil slick. Dark purple thick arrows represent geostrophic winds in the free atmosphere patched to an atmospheric Ekman layer. Red solid arrows denote surface winds at 10 m above the sea surface. Red dashed arrows denote the induced atmospheric secondary circulation. Black solid arrows denote the resultant Ekman transport in the boundary between the water and the oil slick. Black dashed arrows denote the downwelling of the oil slick owing to the net Ekman transport within the boundary.

roughness changes in surface winds and oceanic Ekman transport when the SST gradients are extremely high [~1–5°C $(10\,\text{km})^{-1}$] as observed by Svejkovsky et al. (2012). Figure 13 is a schematic diagram that summarizes the results by depicting an atmospheric secondary circulation and the motion of oil slick under the influence of SST gradient and surface roughness between seawater and an oil slick via Ekman transport.

Analysis from sensitivity experiments indicates our major results are not subject to the selection of ε and the magnitude of forced geostrophic winds. This short study demonstrates the potential effects of oil on the changes to boundary layer processes and hence oil motion itself. These feedbacks from the presence of oil to the oil motion found in this study may be useful for building complex oil-tracking forecast models for future applications. Our results should be validated with field data in future study.

Acknowledgments. This research was made possible in part by a grant from the BP/The Gulf of Mexico Research Initiative (GoMRI), and in part by the National Aeronautics and Space Administration (NASA) Physical Oceanography support of the Ocean Vector Winds Science Team.

REFERENCES

Barth, A., A. Alvera-Azcárate, and R. H. Weisberg, 2008: A nested model study of the Loop Current generated variability and its impact on the west Florida shelf. *J. Geophys. Res.,* **113,** C05009, doi:10.1029/2007JC004492.

Bourassa, M. A., 2006: Satellite-based observations of surface turbulent stress during severe weather. *Atmosphere–Ocean Interactions,* W. Perrie, Ed., Vol. 2, Wessex Institute of Technology Press, 35–52.

——, D. G. Vincent, and W. L. Wood, 1999: A flux parameterization including the effects of capillary waves and sea states. *J. Atmos. Sci.,* **56,** 1123–1139.

Chassignet, E. P., H. E. Hurburt, O. M. Smedstad, G. R. Halliwell, P. J. Hogan, A. J. Wallcraft, R. Baraille, and R. Bleck, 2007: The HYCOM (Hybrid Coordinate Ocean Model) data assimilative system. *J. Mar. Syst.,* **65,** 60–83, doi:10.1016/j.jmarsys.2005.09.016.

Chelton, D. B., 2005: The impact of SST specification on ECMWF surface wind stress fields in the eastern tropical Pacific. *J. Climate,* **18,** 530–550.

——, and F. J. Wentz, 2005: Global microwave satellite observations of sea surface temperature for numerical weather prediction and climate research. *Bull. Amer. Meteor. Soc.,* **86,** 1097–1115.

——, S. K. Esbensen, M. G. Schlax, N. Thum, and M. H. Freilich, 2001: Observations of coupling between surface wind stress and sea surface temperature in the eastern tropical Pacific. *J. Climate,* **14,** 1479–1498.

——, M. G. Schlax, M. H. Freilich, and R. F. Milliff, 2004: Satellite measurements reveal persistent small-scale features in ocean winds. *Science,* **303,** 978–983.

——, ——, and R. M. Samelson, 2007: Summertime coupling between sea surface temperature and wind stress in the California Current system. *J. Phys. Oceanogr.,* **37,** 495–517.

Ekman, V. W., 1905: On the influence of the earth's rotation on ocean currents. *Ark. Mat. Astron. Fys.,* **2** (11), 1–52.

Hénaff, M. L., V. H. Kourafalou, C. B. Paris, J. Helgers, Z. M. Aman, P. J. Hogan, and A. Srinivasan, 2012: Surface evolution of the Deepwater Horizon oil spill patch: Combined effects of circulation and wind-induced drift. *Environ. Sci. Technol.,* **46,** 7267–7273.

Hyun, K. H., and R. He, 2010: Coastal upwelling in the South Atlantic Bight: A revisit of the 2003 cold event using long term observations and model hindcast solutions. *J. Mar. Syst.,* **839** (1–2), 1–13, doi:10.1016/j.jmarsys.2010.05.014.

Ko, D. S., P. J. Martin, C. D. Rowley, and R. H. Preller, 2008: A real-time coastal ocean prediction experiment for MREA04. *J. Mar. Syst.,* **69** (1–2), 17–28, doi:10.1016/j.jmarsys.2007.02.022.

Kondo, J., 1975: Air–sea bulk transfer coefficients in diabatic conditions. *Bound.-Layer Meteor.,* **9,** 91–112.

Liu, Y., R. H. Weisberg, G. Hu, and L. Zheng, 2011: Tracking the Deepwater Horizon oil spill: A modeling perspective. *Eos, Trans. Amer. Geophys. Union,* **92** (6), 45–46.

Maloney, E. D., and D. B. Chelton, 2006: An assessment of the sea surface temperature influence on surface wind stress in numerical weather prediction and climate models. *J. Climate,* **19,** 2743–2762.

Mehra, A., and I. Rivin, 2010: A real time ocean forecast system for the North Atlantic Ocean. *Terr. Atmos. Ocean. Sci.,* **21,** 211–228, doi:10.3319/TAO.2009.04.16.01(IWNOP).

Nikuradse, J., 1933: Strömungsgesetze in rauhen Rohren (Flow laws in rough pipes). V. D. I. Forschungsheft 361, 22 pp.

O'Neill, L. W., D. B. Chelton, and S. K. Esbensen, 2003: Observations of SST-induced perturbations of the wind stress field over the Southern Ocean on seasonal timescales. *J. Climate,* **16,** 2340–2354.

——, ——, and ——, 2005: High-resolution satellite measurements of the atmospheric boundary layer response to SST variations along the Agulhas return current. *J. Climate,* **18,** 2706–2723.

——, ——, and ——, 2010: The effects of SST-induced surface wind speed and direction gradients on midlatitude surface vorticity and divergence. *J. Climate,* **23,** 255–281.

Patoux, J., and R. A. Brown, 2002: A gradient wind correction for surface pressure fields retrieved from scatterometer winds. *J. Appl. Meteor.,* **41,** 133–143.

——, R. C. Foster, and R. A. Brown, 2003: Global pressure fields from scatterometer winds. *J. Appl. Meteor.,* **42,** 813–826.

Robertson, C., and C. Krauss, 2010: Gulf spill is the largest of its kind, scientists say. *New York Times,* 2 August. [Available online at http://www.nytimes.com/2010/08/03/us/03spill.html?_r=0.]

Smith, S. D., and Coauthors, 1992: Sea surface wind stress and drag coefficients: The HEXOS results. *Bound.-Layer Meteor.,* **60,** 109–142.

Song, Q., D. B. Chelton, S. K. Esbensen, N. Thum, and L. W. O'Neill, 2009: Coupling between sea surface temperature and low-level winds in mesoscale numerical models. *J. Climate,* **22,** 146–164.

Stokes, G. G., 1880: On the theory of oscillatory waves. *Mathematical and Physical Papers,* Vol. 1, Cambridge University Press, 197–229.

Svejkovsky, J., W. Lehr, J. Muskat, G. Graettinger, and J. Mullin, 2012: Operational utilization of aerial multispectral remote sensing during oil spill response: Lessons learned during the Deepwater Horizon (MC-252) spill. *Photogramm. Eng. Remote Sens.,* **78,** 1089–1102.

Walker, N. D., W. J. Wiseman Jr., L. J. Rouse Jr., and A. Babin, 2005: Effects of river discharge, wind stress, and slope eddies on circulation and the satellite-observed structure of the Mississippi River plume. *J. Coastal Res.,* **21,** 1228–1244.

Warner, T. T., M. N. Lakhtakia, and J. D. Doyle, 1990: Marine atmospheric boundary layer circulation forced by Gulf Stream sea surface temperature gradients. *Mon. Wea. Rev.,* **118,** 309–323.

Welch, W. M., and C. Joyner, cited 2010: Memorial services honors 11 dead oil rig workers. *USA Today,* 25 May. [Available online at http://usatoday30.usatoday.com/news/nation/2010-05-25-oil-spill-victims-memorial_N.htm.]

Xie, S.-P., 2004: Satellite observations of cool ocean–atmosphere interaction. *Bull. Amer. Meteor. Soc.,* **85,** 195–208.